A&A 386, 415–426 (2002)
DOI: 10.1051/0004-6361:20020221

Astronomy & Astrophysics

The influence of dust on the inverse Compton emission from jets in Active Galactic Nuclei

C. Arbeiter, M. Pohl, and R. Schlickeiser

Institut für Theoretische Physik, Lehrstuhl IV: Weltraum- und Astrophysik, Ruhr-Universität Bochum, 44780 Bochum, Germany

Received 14 February 2001 / Accepted 7 February 2002

Abstract. The recently observed high energy γ-ray emission from more than sixty blazars is most likely caused by inverse Compton scattering of soft ambient photons, the source of which is a subject of extensive debate. We investigate the influence of a dust torus on the inverse Compton emission of the relativistic electrons in the jets of Active Galactic Nuclei. This is an extension of previous studies, in which the main focus had been on target photons emitted by the accretion disk. We show that due to the different angular distribution of the two photon fields, the beaming pattern of the respective scattered inverse Compton gamma rays are different. We also calculate the bolometric luminosity, the beaming pattern and the spectral distribution of the emitted gamma rays for the dust torus as well as for the accretion disk as the target photon source. The results show that the relative contributions of both to the gamma ray emission depend sensitively on the observer's viewing angle and the distance of the jet plasmoids from the accretion disk and the dust torus, respectively.

Key words. radiation mechanisms: non-thermal – quasars: general – gamma rays: theory

1. Introduction

The first AGNi were discovered about 40 years ago after optical identification of powerful, compact and variable radio sources (Schmidt 1963). Later high resolution radio observations exhibited structured jets feeding the large radio lobes; in some cases the apparent bulk velocities of the source components exceeds the speed of light: the so called superluminal motion (Cohen et al. 1977; Gomez et al. 1998). The energy radiated by the AGNi during their lifetime and the apparent stability of the jet axis seem to require that the central engine is a super massive black hole (Begelman et al. 1984).

This motivate the picture of discrete plasmoids, subsequently denoted as blobs, travelling outwards from the central region along the angular momentum axis of the black hole with a velocity close to the speed of light. Thus the superluminal motion and the enormous luminosity of the most conspicuous subclass of AGNi, the blazars, can be explained by Doppler boosting towards favourably aligned observers. The angular dependence of the Doppler boosting together with the assumption of a dust torus surrounding the central region of the AGNi, which would absorb the X-rays from the accretion disk, should be able to explain most of the phenomenology of AGNi (for review see Urry & Padovani 1995). Accordingly the angle between the jet axis and the line of sight determines the classification of the AGNi.

It came as a surprise when, a decade ago, EGRET aboard the Compton Gamma Ray Observatory detected many blazars as strong and variable γ-ray emitters (von Montigny et al. 1995; Mukherjee et al. 1997). More recently, observations with ground-based Čerenkov telescopes have shown that at least for BL Lacertae objects the γ-ray spectrum can be traced to more than a TeV observed photon energy (Punch et al. 1992; Quinn et al. 1996; Catanese et al. 1998; Krennrich et al. 1997). In these sources the bulk of luminosity is often emitted in the form of γ-rays.

The inverse Compton scattering has been considered a likely mechanism to produce the high energy γ-radiation from AGNi ever since *COS B* detected the first extragalactic γ-ray source, 3C 273. In this process low energy photons are scattered by relativistic electrons within the jets. The low energy photons may penetrate the jet from outside, for example from the accretion disk of the central black hole, this process being named *External-Inverse-Compton scattering (EIC)* (e.g. Dermer et al. 1992), or they can be generated by the jet itself via synchrotron radiation, the *Synchrotron-Self-Compton scattering (SSC)* (e.g. Maraschi et al. 1992).

Blazars can be divided into two subclasses: BL Lacertae objects and flat spectrum radio quasars or optically violent variables, FSRQ/OVV. It would

Send offprint requests to: C. Arbeiter,
e-mail: ca@tp4.ruhr-uni-bochum.de

seem that in BL Lacertae objects, in the absence of a strong external photon field, the SSC process dominates (Mastichiadis & Kirk 1997; Ghisellini et al. 1998; Coppi & Aharonian 1999), whereas in case of the FSRQ/OVV the EIC process is more important.

Some of the observed blazars show little variation in the γ-ray flux over periods of weeks which, in the framework of EIC models, can be easily understood if the external photon field is rather homogeneous on scales of 10^{17}–10^{18} cm. Some variants of the EIC models have therefore considered thick accretion disks (Bednarek & Kirk 1995) or photons backscattered by clouds in the broad line region (Sikora et al. 1994).

Observations of AGNi in the infra-red range show spectral features which can be interpreted as thermal dust emission. Because the thermal emission is supposedly isotropic, the luminosities can be enormous. In the case of PG 1247+267 Haas et al. (1998, 2000) find $L_{\mathrm{IR}} \approx 2 \times 10^{14} L_{\odot}$, which is more than 50 times brighter than the Eddington luminosity of a black hole of $10^8\, M_{\odot}$. Therefore it would seem that the dust torus is an important source of target photons for the γ-ray production. At the same time photon-photon absorption on dust emission would prevent the escape of TeV photons, which have been produced within the vertical extent of the dust torus (Protheroe & Biermann 1997).

Recently, Błażejowski et al. (2000) have calculated γ-ray spectra from comptonisation of dust emission for a specific line-of-sight to the observer ($\theta_{\mathrm{obs}} = 1/\Gamma$). In this paper we will derive analytical solutions for the comptonisation spectra of dust emission for arbitrary observing angles. Our study does not rely on a specific model for the injection or acceleration of relativistic electrons in the jets of AGN. Therefore our results can also be used to determine EIC spectra in blast wave models for AGN and GRB (Pohl & Schlickeiser 2000).

The paper is organized as follows: in Sect. 2 we will specify the notation used in the following sections as well as the geometry, and we will outline the basic idea of the following calculations; in Sect. 3 we shall calculate the differential scattering rate $\dot{n}_{\mathrm{S}}$ for an arbitrary placed point source for both a monochromatic and a grey-body target photon distribution; in Sects. 4 and 5 we will calculate the resultant differential luminosity, the beaming pattern and shall expand the solutions to extended sources, respectively. In Sect. 6 we derive the differential photon number spectrum of an extended source in the case of a monochromatic target photon source. Section 7 gives a summary.

2. General considerations

Figure 1 shows a sketch of the situation: the collimated outflow in the jets is not continuous but bunched to discrete plasmoids subsequently denoted as blobs. These move along the angular-momentum axis of the central black hole and perpendicular to its associated accretion disc. Photons of a point source of thermal radiation at an arbitrary point H will penetrate the blob and be scattered

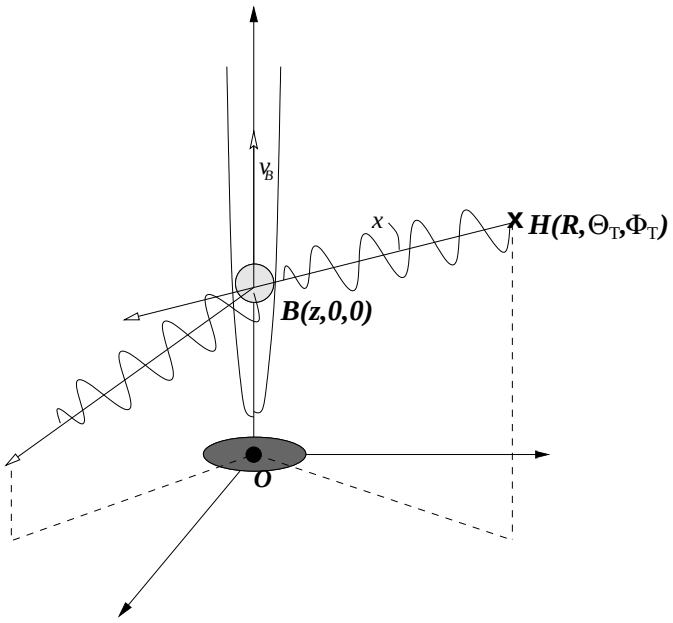

Fig. 1. Sketch of the basic geometry: the central black hole defines the point of origin O of the system of coordinates. A photon, emitted at an arbitrary Point H with the spherical polar coordinates R, Θ_{Γ} and Φ_{Γ}, is scattered within the blob at point B which is situated at the distance z above the black hole and moves along its angular momentum axis with velocity $v_{\mathrm{B}} = B_{\Gamma} c$ and the associated Lorentz factor Γ. In a frame centered on the point B, point H has coordinates x, $\pi - \Theta_{\mathrm{H}}$ and Φ_{H}.

by the high relativistic electrons and positrons within the blob and thereby gain energy. The energy gain depends on the geometrical relations as well as on the blob's and electron's/positron's Lorentz factors.

In general all quantities in the electron rest frame are indicated by a prime and those in the frame of the galaxy by an asterisk; quantities in the blob rest frame are not indexed. For simplicity we will perform the calculus in the rest frame of the blob. Therefore all quantities have to be transformed into the blob frame which we do with the help of relativistic invariants. In the same way the results can be transformed into the frame of the galaxy respectively, and using a particular cosmological model, into the frame of the observer.

We will first calculate the scattering rate for an arbitrarily placed point source; then the solution for an extended source can be derived by integrating the solution for a point source over the source distribution.

3. The differential scattering rate

The differential scattering rate, which is the angle-dependent photon number spectrum of the scattered photons, is in the blob frame given by (Dermer et al. 1992)

$$\dot{n}_{\mathrm{S}}(\epsilon_{\mathrm{S}}, \Omega_{\mathrm{S}}) = c \int_0^{\infty} \mathrm{d}\epsilon \oint \mathrm{d}\Omega \int_1^{\infty} \mathrm{d}\gamma \oint \mathrm{d}\Omega_{\mathrm{e}} \times (1 - \beta \cos\psi)\, n_{\mathrm{ph}}(\epsilon, \Omega)\, n_{\mathrm{e}}(\gamma, \Omega_{\mathrm{e}})\, \frac{\mathrm{d}^2\sigma}{\mathrm{d}\epsilon_{\mathrm{S}} \mathrm{d}\Omega_{\mathrm{S}}}. \quad (1)$$

Here, $n_{\rm ph}$ and $n_{\rm e}$ denote the differential number density of the incoming photons and the blob electrons, respectively. Since the scattering process is charge-independent, we don't distinguish electrons and positrons. The differential cross section $\mathrm{d}^2\sigma/(\mathrm{d}\epsilon_{\rm S}\mathrm{d}\Omega_{\rm S})$ can be written in the Thomson limit ($\epsilon' = \gamma\epsilon(1-\beta\cos\psi) \leq 1$) with the help of the head-on approximation as (Reynolds 1982; Dermer & Schlickeiser 1993)

$$\frac{\mathrm{d}^2\sigma}{\mathrm{d}\epsilon_{\rm S}\mathrm{d}\Omega_{\rm S}} = \sigma_{\rm T}\delta\Big[\epsilon_{\rm S} - \gamma^2\epsilon(1-\beta\cos\psi)\Big] \times \delta(\mu_{\rm S}-\mu_{\rm e})\,\delta(\phi_{\rm S}-\phi_{\rm e}), \quad (2)$$

where ψ is the angle between the incoming photons and the blob electrons and $\mu_{\rm i}$ denotes the cosine of the corresponding angle $\Theta_{\rm i}$, respectively. In the frame of the galaxy the thermal photon point source at H provides a photon number density at the place B of

$$n^*_{\rm H}(\epsilon^*,\mu^*,\phi^*) = \frac{\dot{N}_{\rm H}(\epsilon^*)}{4\pi x^2 c}\,\delta(\mu^*-\mu^*_{\rm H})\,\delta(\phi^*-\phi^*_{\rm H}), \quad (3)$$

where x denotes the distance between the photon source at H and the blob at B (cf. Fig. 1). $\dot{N}_{\rm H}$ is the photon number spectrum of the photon source and c means the speed of light. Using the invariance of n/ϵ^2 (Rybicki & Lightman 1979) and the transformation properties of ϵ^* and μ^* (Hagedorn 1973)

$$\epsilon^* = \Gamma\epsilon(1+B_\Gamma\mu), \quad \mu^* = \frac{\mu+B_\Gamma}{1+B_\Gamma\mu}. \quad (4)$$

Equation (3) can be transformed to the rest frame of the blob:

$$n_{\rm H}(\epsilon,\mu,\phi) = \frac{\dot{N}_{\rm H}\big(\Gamma\epsilon(1+B_\Gamma\mu_0)\big)}{4\pi x^2 c}\delta(\mu-\mu_0)\,\delta(\phi-\phi_{\rm H}), \quad (5)$$

$$\mu_0 \equiv \frac{\mu^*_{\rm H}-B_\Gamma}{1-B_\Gamma\mu^*_{\rm H}}. \quad (6)$$

Assuming an isotropic power law energy distribution with a low and an high energy cut-off for the electrons within the blob,

$$n_{\rm e}(\gamma,\Omega_{\rm e}) = \frac{n_{\rm e}(\gamma)}{4\pi} = \frac{n_0}{4\pi}\,\gamma^{-s}, \qquad \gamma_1 \leq \gamma \leq \gamma_2, \quad (7)$$

performing the integral in Eq. (1), the transformation into the galactic frame, here using the invariance $\dot{n}/\epsilon$, leads to

$$\dot{n}^*_{\rm S}(\epsilon^*_{\rm S},\Omega^*_{\rm S}) = \frac{D\sigma_{\rm T}\,n_0}{16\pi^2x^2}\int_{\gamma_1}^{\gamma_2}\mathrm{d}\gamma\;\gamma^{-(s+2)}\dot{N}_{\rm H}\left(\frac{\epsilon^*_{\rm S}}{\eta\,\gamma^2}\right), \quad (8)$$

where D denotes the Doppler factor $D \equiv [\Gamma(1-B_\Gamma\mu^*_{\rm S})]^{-1}$ and

$$\eta \equiv \frac{D(1-\beta\cos\psi_0)}{\Gamma(1+B_\Gamma\mu_0)} \overset{\beta\to1}{\simeq} D^2\Big[1-\mu^*_{\rm S}\mu^*_{\rm H} - \sqrt{(1-\mu^{*2}_{\rm S})(1-\mu^{*2}_{\rm H})}\,\cos(\phi^*_{\rm S}-\phi^*_{\rm H})\Big]. \quad (9)$$

Thus, η contains the geometrical information of the scattering process. The constant n_0 in Eq. (7) is related to the total number density of the electrons $n^{(0)}_{\rm e}$ by

$$n_0 = n^{(0)}_{\rm e}\begin{cases}\frac{1-s}{\gamma_2^{1-s}-\gamma_1^{1-s}}, & s\neq1\\ 1/\ln(\frac{\gamma_2}{\gamma_1}), & s=1\end{cases} \quad (10)$$

and the cosine $\cos\psi_0$ in (9) is defined as

$$\cos\psi_0 \equiv \mu_0\mu_{\rm S} + \sqrt{(1-\mu_0^2)(1-\mu_{\rm S}^2)}\,\cos(\phi_{\rm S}-\phi_0). \quad (11)$$

At this point we need to specify the photon number spectrum of the photon source. We consider a grey body (GB) as well as a monochromatic (MC) photon spectrum:

$$\dot{N}_{\rm H}(\epsilon^*) = \begin{cases}\dot{N}^{(0)}_{\rm H}\,\frac{\epsilon^{*2}}{\mathrm{e}^{\frac{\epsilon^*}{\Theta}}-1}\,\frac{1}{2\,\zeta(3)\,\Theta^3}, & \text{GB}\\ \dot{N}^{(0)}_{\rm H}\,\delta(\epsilon^*-\langle\epsilon^*\rangle), & \text{MC.}\end{cases} \quad (12)$$

Here, $\Theta = k_{\rm B}T/(m_{\rm e}c^2)$ is the dimensionless temperature of the emitter and $\langle\epsilon^*\rangle$ is the mean energy of the grey body spectrum

$$\langle\epsilon^*\rangle = \frac{\int_0^\infty \mathrm{d}\epsilon^*\;\epsilon^*\,\dot{N}_{\rm H}(\epsilon^*)\Big|_{\rm GB}}{\int_0^\infty \mathrm{d}\epsilon^*\;\dot{N}_{\rm H}(\epsilon^*)\Big|_{\rm GB}} = \frac{\Gamma(4)\,\zeta(4)}{\Gamma(3)\,\zeta(3)}\,\Theta, \quad (13)$$

where ζ denotes the Riemann zeta function (Gradshteyn & Ryzhik 1965).

In the case of a grey body photon source we obtain for the differential scattering rate

$$\dot{n}^*_{\rm S}(\epsilon^*_{\rm S},\Omega^*_{\rm S})\Big|_{\rm GB} = \frac{D\,\sigma_{\rm T}\,n_0\,\dot{N}^{(0)}_{\rm H}}{64\,\pi^2x^2\,\zeta(3)\,\Theta}\left(\frac{\epsilon^*_{\rm S}}{\eta\,\Theta}\right)^{-\frac{s+1}{2}} \times \int_{\frac{\epsilon^*_{\rm S}}{\eta\Theta\gamma_2^2}}^{\frac{\epsilon^*_{\rm S}}{\eta\Theta\gamma_1^2}}\mathrm{d}t\frac{t^{\frac{s+3}{2}}}{\mathrm{e}^t-1}, \quad (14)$$

whereas in the case of a monochromatic photon source we find

$$\dot{n}^*_{\rm S}(\epsilon^*_{\rm S},\Omega^*_{\rm S})\Big|_{\rm MC} = \frac{D\,\sigma_{\rm T}\,n_0\,\dot{N}^{(0)}_{\rm H}}{32\,\pi^2x^2\,\langle\epsilon^*\rangle}\left(\frac{\epsilon^*_{\rm S}}{\eta\,\langle\epsilon^*\rangle}\right)^{-\frac{s+1}{2}} \quad \text{for } \eta\,\langle\epsilon^*\rangle{\gamma_1}^2 \leq \epsilon^*_{\rm S} \leq \eta\,\langle\epsilon^*\rangle{\gamma_2}^2. \quad (15)$$

The restriction in energy is a consequence of the cut-offs in the energy spectrum of the radiating electrons (cf. Eq. (7)). This result is in accordance to the result of Dermer & Schlickeiser (1993) for η averaged over $\phi_{\rm H}$. With Eqs. (14, 15) we can calculate the differential photon number spectrum for target photons of an extended source by integration over the source distribution. Afterwards, the

differential luminosity, i.e. the luminosity per solid angle element, can be derived by an energy integration. Since the integral over the source distribution is much simpler when the energy integration is performed first, we will first derive the differential luminosity for a point source and then for an extended target photon source. The calculation of the differential photon number spectrum is performed in Sect. 6.

4. The differential luminosity $\mathrm{d}L^*_\mathrm{S}/\mathrm{d}\Omega^*_\mathrm{S}$

The differential luminosity of the scattered photons in the galactic frame can be derived from

$$\frac{\mathrm{d}L^*_\mathrm{S}}{\mathrm{d}\Omega^*_\mathrm{S}} = m_\mathrm{e}c^2 D V_\mathrm{B} \int_0^\infty \mathrm{d}\epsilon^*_\mathrm{S}\, \epsilon^*_\mathrm{S}\, \dot{n}^*_\mathrm{S}, \tag{16}$$

with the volume of the blob, $V^*_\mathrm{B} = DV_\mathrm{B}$ (Begelman et al. 1984). Inserting the derived solution for $\dot{n}^*_\mathrm{S}$ from Eqs. (8) with (13) in (16), we get the same differential luminosity for the monochromatic photon source as well as for a grey body spectrum.

$$\frac{\mathrm{d}L^*_\mathrm{S}}{\mathrm{d}\Omega^*_\mathrm{S}} = \frac{3}{16\pi^2}\, m_\mathrm{e}c^2 V_\mathrm{B}\, \sigma_\mathrm{T}\, n_0\, \dot{N}^{(0)}_\mathrm{H}\, \Theta \frac{\zeta(4)}{\zeta(3)}\, D^2 \times \frac{\eta^2}{x^2} \begin{cases} \frac{{\gamma_2}^{3-s} - {\gamma_1}^{3-s}}{3-s}, & s \neq 3 \\ \ln\left(\frac{\gamma_2}{\gamma_1}\right), & s = 3. \end{cases} \tag{17}$$

Thus the assumption of a monochromatic photon source as an approximation of a photon source radiating with a thermal spectrum has no impact on the differential luminosity of the inverse Compton scattered photons.

The differential luminosity of an extended photon source can be derived by integrating over its surface provided that the photon source is either geometrically thin or optically thick. Here we simplify the dust torus as an infinitely thin belt with constant distance to the black hole, R_DT, and finite extent in polar angle with $-\tau \leq \mu^*_\mathrm{T} \leq \tau$. We have to distinguish between optically thin and optically thick emission. In the optically thick case the cosine of the angle between the normal of the emitter surface and the direction to the blob has to be taken into account. With

$$\rho_\mathrm{m} \equiv \begin{cases} \frac{{\gamma_2}^{m-s} - {\gamma_1}^{m-s}}{m-s}, & s \neq m \\ \ln\left(\frac{\gamma_2}{\gamma_1}\right), & s = m \end{cases} \tag{18}$$

in the optically thin case we then obtain for the scattered dust torus emission

$$\left.\frac{\mathrm{d}L^*_\mathrm{S}}{\mathrm{d}\Omega^*_\mathrm{S}}\right|^{\mathrm{thin}}_{\mathrm{DT}} = \frac{3}{16\pi^2}\, m_\mathrm{e}c^2 V_\mathrm{B}\, \sigma_\mathrm{T}\, n^{(0)}_\mathrm{e}\, (\dot{N}^{(0)}_\mathrm{H}\, \Theta)_\mathrm{DT} \frac{\rho_3}{\rho_1} \frac{\zeta(4)}{\zeta(3)}\, D^2 \times R^2_\mathrm{DT} \int_{-\tau}^{\tau} \mathrm{d}\mu^*_\mathrm{T} \int_0^{2\pi} \mathrm{d}\phi^*_\mathrm{T}\, \frac{\eta^2}{x^2}. \tag{19}$$

Note that n_0 in (10) can be represented as $n^{(0)}_\mathrm{e}/\rho_1$. Inserting η from (9) and making use of the relations

$$\begin{aligned} x^2 &= R^2_\mathrm{DT} + z^2 - 2zR_\mathrm{DT}\mu^*_\mathrm{T}\,, \\ \mu^*_\mathrm{H} &= \frac{f - \mu^*_\mathrm{T}}{\sqrt{1 + f^2 - 2\, f\, \mu^*_\mathrm{T}}}\,, \\ \phi^*_\mathrm{T} &= \phi^*_\mathrm{H}\,, \end{aligned} \tag{20}$$

where $f \equiv z/R_\mathrm{DT}$ is the height of the blob, z, normalised to the radius of the dust torus, R_DT, we get

$$\left.\frac{\mathrm{d}L^*_\mathrm{S}}{\mathrm{d}\Omega^*_\mathrm{S}}\right|^{\mathrm{thin}}_{\mathrm{DT}} = \frac{3}{16\pi}\, m_\mathrm{e}c^2 V_\mathrm{B}\, \sigma_\mathrm{T}\, n^{(0)}_\mathrm{e}\, (\dot{N}^{(0)}_\mathrm{H}\, \Theta)_\mathrm{DT} \frac{\rho_3}{\rho_1} \frac{\zeta(4)}{\zeta(3)}\, D^6 \times \frac{1}{f} \left[\frac{3{\mu^*_\mathrm{S}}^2 - 1}{8f^2} \mathrm{K}^{(2)}_+ - 2\, \frac{\mu^*_\mathrm{S}}{f} \mathrm{K}^{(1)}_- + \left(3 - {\mu^*_\mathrm{S}}^2 - (1 - f^2) \frac{3{\mu^*_\mathrm{S}}^2 - 1}{2f^2}\right) \ln\left(\frac{o}{u}\right) \right] \tag{21}$$

with $o \equiv \sqrt{f^2 + 1 + 2f\tau}$, $u \equiv \sqrt{f^2 + 1 - 2f\tau}$ and

$$\mathrm{K}^{(n)}_\pm \equiv \left(1 \pm \frac{(1 - f^2)^n}{o^n u^n}\right)(o^n - u^n). \tag{22}$$

For an accretion disk of radial size R_AD and inner radius R_I located at $z = 0$ we calculate correspondingly

$$\left.\frac{\mathrm{d}L^*_\mathrm{S}}{\mathrm{d}\Omega^*_\mathrm{S}}\right|^{\mathrm{thin}}_{\mathrm{AD}} = \frac{3}{16\pi^2}\, m_\mathrm{e}c^2 V_\mathrm{B}\, \sigma_\mathrm{T}\, n^{(0)}_\mathrm{e} \frac{\rho_3}{\rho_1} \frac{\zeta(4)}{\zeta(3)}\, D^2 \times \int_{R_\mathrm{I}}^{R_\mathrm{AD}} \mathrm{d}R \int_0^{2\pi} \mathrm{d}\phi^*_\mathrm{T}\, R\, \frac{\eta^2}{x^2}\, (\dot{N}^{(0)}_\mathrm{H}\Theta)_\mathrm{AD}(R). \tag{23}$$

Here, Θ_AD and $\dot{N}^{(0)}_\mathrm{H}$ depend on the radius. For the bolometric flux

$$\begin{aligned} B(R) &= m_\mathrm{e}c^2 (\dot{N}^{(0)}_\mathrm{H} \langle\epsilon^*\rangle)_\mathrm{AD}(R) \\ &= 3\frac{\zeta(4)}{\zeta(3)} m_\mathrm{e}c^2 (\dot{N}^{(0)}_\mathrm{H}\Theta)_\mathrm{AD}(R) \end{aligned} \tag{24}$$

we use the model of Shakura & Sunyaev (1973)

$$B(R) = \frac{3}{8\pi} \frac{GM^2_\odot}{a}\, R^{-3} \left(\frac{M}{M_\odot}\right) \left(\frac{\dot{M}}{M_\odot/a}\right) \varphi\,, \tag{25}$$

where $a \simeq 3.15 \times 10^7$ s denotes one year in seconds, M the mass and $\dot{M}$ the mass accretion rate of the black hole, respectively, and

$$\varphi \equiv \left[1 - \sqrt{\frac{3R_\mathrm{S}}{R}}\right] \qquad \text{with} \qquad R_\mathrm{S} = 2\, GM/c^2, \tag{26}$$

the Schwarzschild radius. A good approximation is given by

$$\varphi \simeq q \left[1 - \frac{bR_\mathrm{S}}{R}\right]. \tag{27}$$

with $q = 0.75, b = 3.4$ and a lower integration limit of $R_I = 4R_S$. With

$$\mu_H^* = \frac{z}{\sqrt{z^2+R^2}}\,, \quad F \equiv z/R_{AD}, \tag{28}$$

where F is the height z normalised to the radius of the accretion disk, R_{AD}, we obtain

$$\left.\frac{dL_S^*}{d\Omega_S^*}\right|_{AD}^{thin} = \frac{3q\,V_B\,\sigma_T\,n_e^{(0)}}{64\pi^2 R_{AD}^3}\,\frac{\rho_3}{\rho_1}\frac{GM_\odot^2}{a}\left(\frac{M}{M_\odot}\right)\left(\frac{\dot{M}}{M_\odot/a}\right)$$
$$\times\; D^6\,F^{-3}\Bigg[\mathrm{M}\left(\mu_S^*, F\frac{R_I}{R_{AD}}\right) - \mathrm{M}(\mu_S^*, F)$$
$$-\frac{1}{2}\frac{bR_S}{R_{AD}F}\left(\mathrm{N}(\mu_S^*, F\frac{R_I}{R_{AD}}) - \mathrm{N}(\mu_S^*, F)\right)\Bigg], \tag{29}$$

where we define

$$\mathrm{M}(\mu_S^*, y) \equiv (1+\mu_S^{*2})\,y - 2\mu_S^*\frac{y^2+2}{\sqrt{1+y^2}}$$
$$-\;\frac{1}{4}(7\mu_S^{*2}+3)\mathrm{arctan}(y) + \frac{1}{4}(3\mu_S^{*2}-1)\frac{y}{1+y^2}\,, \tag{30}$$

$$\mathrm{N}(\mu_S^*, y) \equiv (1+\mu_S^{*2})\,y^2 - 2\mu_S^*\left[\frac{y(y^2+3)}{\sqrt{1+y^2}} - 3\,\mathrm{arcsinh}(y)\right]$$
$$-\;\frac{1}{2}(5\mu_S^{*2}+1)\ln(1+y^2) + \frac{1}{2}(3\mu_S^{*2}-1)\frac{1}{1+y^2}\cdot \tag{31}$$

In the optically thick case the angle between the normal of the surface and the direction to the blob has to be taken into account. For the scattered dust torus emission we get (cf. Eq. (19))

$$\left.\frac{dL_S^*}{d\Omega_S^*}\right|_{DT}^{thick} \propto \int_{-\tau}^{\tau} d\mu_T^* \int_0^{2\pi} d\phi_T^*\,\frac{\eta^2}{x^2}\,\mu_K^*\,, \tag{32}$$

where μ_K^* is the cosine of the angle $\angle(\overline{\boldsymbol{HB}}, \overline{\boldsymbol{HO}})$ (cf. Fig. 1)

$$\mu_K^* = \frac{1-f\mu_T^*}{\sqrt{1+f^2-2\,f\,\mu_T^*}}. \tag{33}$$

The calculation leads to

$$\left.\frac{dL_S^*}{d\Omega_S^*}\right|_{DT}^{thick} = \frac{3}{32\pi}\,m_e c^2 V_B\,\sigma_T\,n_e^{(0)}\,(\dot{N}_H^{(0)}\,\Theta)_{DT}\frac{\rho_3}{\rho_1}\frac{\zeta(4)}{\zeta(3)}\,D^6$$
$$\times\,\frac{1}{f}\left[\frac{3\mu_S^{*2}-1}{12f^2}\,\mathrm{K}_+^{(3)} - \frac{\mu_S^*}{f}\,\mathrm{K}_-^{(2)}\right.$$
$$\left.+\left(3-\mu_S^{*2}-(1-f^2)\frac{3\mu_S^{*2}-1}{4f^2}\right)\mathrm{K}_+^{(1)}\right]. \tag{34}$$

For the definition of $\mathrm{K}_\pm^{(n)}$ see (22). Correspondingly we get for the comptonised optically thick accretion disk radiation

$$\left.\frac{dL_S^*}{d\Omega_S^*}\right|_{AD}^{thick} \propto \int_{R_I}^{R_{AD}} dR \int_0^{2\pi} d\phi_T^*\,R\,\frac{\eta^2}{x^2}\,(\dot{N}_H^{(0)}\Theta)_{AD}(R)\,\mu_H^* \tag{35}$$

which leads to a slightly modified solution compared to the optically thin case

$$\left.\frac{dL_S^*}{d\Omega_S^*}\right|_{AD}^{thick} = \frac{3q\,V_B\,\sigma_T\,n_e^{(0)}}{64\pi^2 R_{AD}^3}\,\frac{\rho_3}{\rho_1}\frac{GM_\odot^2}{a}\left(\frac{M}{M_\odot}\right)\left(\frac{\dot{M}}{M_\odot/a}\right)$$
$$\times\; D^6\,F^{-3}\Bigg[\mathrm{P}\left(\mu_S^*, F\frac{R_I}{R_{AD}}\right) - \mathrm{P}(\mu_S^*, F)$$
$$-\frac{1}{2}\frac{bR_S}{R_{AD}F}\left(\mathrm{Q}\left(\mu_S^*, F\frac{R_I}{R_{AD}}\right) - \mathrm{Q}(\mu_S^*, F)\right)\Bigg], \tag{36}$$

where we define

$$\mathrm{P}(\mu_S^*, y) \equiv (1+\mu_S^{*2})\,\frac{y^2+2}{\sqrt{1+y^2}} - \frac{1}{2}(3\mu_S^{*2}-1)\frac{3y^2+2}{(1+y^2)^{\frac{3}{2}}}$$
$$-\,2\mu_S^*\left[y + \frac{1}{2}\,\frac{y}{1+y^2} - \frac{3}{2}\mathrm{arctan}(y)\right], \tag{37}$$

$$\mathrm{Q}(\mu_S^*, y) \equiv (1+\mu_S^{*2})\,\frac{y(y^2+3)}{\sqrt{1+y^2}} - (6\mu_S^{*2}+2)\,\mathrm{arcsinh}(y)$$
$$-\,2\mu_S^*\left[y^2 + \frac{1}{1+y^2} - 2\ln(1+y^2)\right]$$
$$+\,(3\mu_S^{*2}-1)\left[\frac{1}{3}\frac{y^3}{(1+y^2)^{\frac{3}{2}}} + \frac{y}{\sqrt{1+y^2}}\right]. \tag{38}$$

Figure 2 shows the dependence of the differential luminosity in arbitrary units on the aspect angle Θ_S^* as polar plot for the dust torus (solid line) and the accretion disk (dash-dotted line) as optically thin target photon sources in different distances of the blob from the centre, F. The 0° direction defines the jet axis. The aspect angle Θ_S^* corresponds to the angle between the line of sight of an observer and the jet axis of the AGNi. We use $L_{DT}/L_{AD} = 15$, which is in accordance with the ratio of an intermediate dust luminosity measured by Haas et al. (1998) and an accretion disk luminosity estimated by the Eddington luminosity of a black hole of $10^8 M_\odot$, i.e. $L_{AD} = 1.3\times10^{46}\,\mathrm{erg\,s^{-1}}$. Furthermore we choose $s=3$, $R_{DT}/R_{AD} = 1000$, i.e. $f = F/1000$, $R_I/R_{AD} = 4/300$ and, here, for presentability $\Gamma = 2.3$. The opening angle of the dust torus is $\Theta_\tau^* = 60°$, corresponding to $\tau = 0.5$. The left panel of Fig. 2 shows an antenna diagram for a distance $F=4$; the maximum of the cone-like angular distribution of the scattered accretion disk emission dominates the differential luminosity for observing angles of $\Theta_S^* \approx \Theta_S^{*\max}$ (cf. Fig. 5). For small aspect angles the differential luminosity is clearly dominated by the scattered dust emission. At a distance $F=7$ (right panel) the dust torus has even become more important and stays dominant for greater distances because the accretion disk photon field decays as F^{-2}. The relative intensities of the two components scale with the luminosities of the accretion disk and the dust torus, that is with L_{DT}/L_{AD}. Were the dust torus less luminous, the scattered accretion disk emission would provide the absolute maximum of the differential luminosity

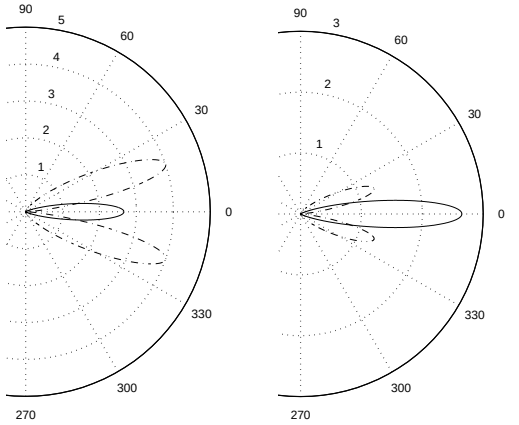

Fig. 2. The differential luminosity in arbitrary units as antenna diagrams for the dust torus (solid line) and the accretion disk (dash-dotted line) as optically thin target photon sources for different distances of the blob from the centre, F, measured in units of the accretion disk radius. The 0° direction defines the jet axis. Here we use an electron spectral index $s = 3$ and for presentability $\Gamma = 2.3$; for other parameters, see the text. *Left panel*: $F = 4$; the scattered accretion disk emission dominates the differential luminosity, whereas for small angles the scattered dust emission is more intense than the accretion disk contribution. *Right panel*: $F = 7$; the scattered dust emission yields the absolut maximum of the differentiel luminosity and stays dominant also for greater distances. Note that the relative intensities of the two components scale with $L_{\rm DT}/L_{\rm AD}$.

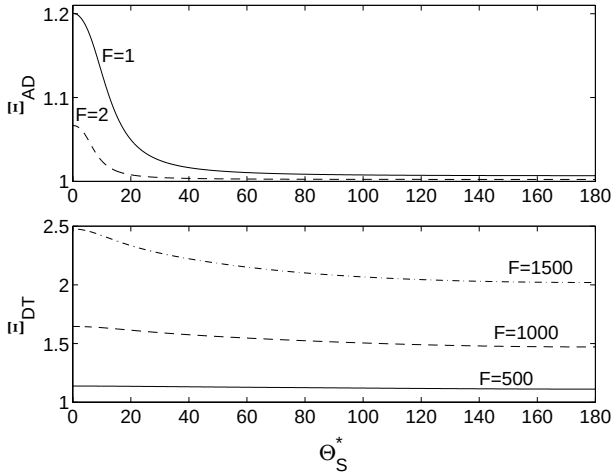

Fig. 3. The quotient Ξ of the differential luminosities in the optically thin and the optically thick case for the accretion disk (upper panel) and the dust torus (lower panel) as target photon sources as a function of the distance of the blob from the centre, F, measured in units of the accretion disk radius. For both target photon emitters the difference shows a marginal angle-dependence. *Upper panel*: for the accretion disk the additional factor $\mu_{\rm H}^*$ is approximately unity for $F \gg 1$ and therefore likewise $\Xi_{\rm AD} \approx 1$. Thus the differential luminosities differ only near to the accretion disk distinctly. *Lower panel*: for the dust torus the difference between the optically thin and the optically thick solution of the differential luminosity becomes largest when the additional factor $\mu_{\rm K}^*$ in the integrand of the optically thick case becomes small for photons emitted from the upper edge of the dust torus, i.e. for $f\tau \to 1$. (Here, $\tau = 0.5$, $F = 1000$ f).

also at distances somewhat larger than $F = 7$. However, the different antenna patterns would persist: the scattered dust emission is concentrated in the exact forward direction, $\Theta_{\rm s}^* = 0°$, and yields the main contribution whereas the scattered accretion disk emission is most intense for intermediate aspect angles, $\Theta_{\rm S}^* \approx 1/\Gamma$.

Figure 3 shows the difference between optically thin and optically thick target photon sources on the differential luminosities. The quotient Ξ of the differential luminosities shows a weak angle-dependence. For the accretion disk (upper panel) the additional factor $\mu_{\rm H}^*$ is approximately unity for $F \gg 1$ and therefore likewise $\Xi_{\rm AD} \approx 1$. Thus the differential luminosities differ distinctly only near to the accretion disk. For the dust torus (lower panel) the difference between the optically thin and the optically thick solution of the differential luminosity becomes largest when the blob sees target photons from the upper edge of the dust torus which have been emitted obliquely to the surface of the dust torus, i.e. for $f\tau \to 1$.

5. The beaming pattern

The beaming pattern shows the relative contribution of the two target photon sources independent of their luminosity. To derive the beaming pattern, we have to normalise the differential luminosity of the scattered photons to the differential luminosity of the target photon source, respectively.

$$S = \frac{\frac{{\rm d}L_{\rm S}^*}{{\rm d}\Omega_{\rm S}^*}}{\frac{{\rm d}L_{\rm H}^*}{{\rm d}\Omega_{\rm S}^*}}, \qquad \frac{{\rm d}L_{\rm H}^*}{{\rm d}\Omega_{\rm S}^*} = \frac{m_{\rm e}c^2}{4\pi} \int {\rm d}A \int_0^\infty {\rm d}\epsilon^* \, \epsilon^* \dot{N}_{\rm H} \, . \tag{39}$$

For the target photon source luminosity we find in the case of the accretion disk with (12) and the relations for the flux used in the previous chapter

$$\left.\frac{{\rm d}L_{\rm H}^*}{{\rm d}\Omega_{\rm S}^*}\right|_{\rm AD}^{\rm thin} = \frac{3}{16\pi}\frac{GM_\odot^2}{a}\left(\frac{M}{M_\odot}\right)\left(\frac{\dot{M}}{M_\odot/a}\right) \times \frac{R_{\rm AD}-R_{\rm I}}{R_{\rm AD}R_{\rm I}}\left[1-\frac{bR_{\rm S}}{2}\frac{R_{\rm AD}+R_{\rm I}}{R_{\rm AD}R_{\rm I}}\right]. \tag{40}$$

In the optically thick case the optically thin solution has to be multiplied with the cosine of the aspect angle $\mu_{\rm S}^*$ to take into account that the effective area of the accretion disk seen in the $\Theta_{\rm S}^*$ direction varies with $\mu_{\rm S}^*$. For the dust emission we derive

$$\left.\frac{{\rm d}L_{\rm H}^*}{{\rm d}\Omega_{\rm S}^*}\right|_{\rm DT}^{\rm thin} = 3\frac{\zeta(4)}{\zeta(3)} m_{\rm e}c^2 \left(\dot{N}_{\rm H}^{(0)}\,\Theta\right)_{\rm DT} R_{\rm DT}^2\,\tau. \tag{41}$$

For optically thick dust emission the integrand in (39) becomes a complicated function of $\mu_{\rm T}^*$. In the special case $\tau = 1$, τ is the cosine of the finite extent in polar angle of the dust, an easier solution can be found which corresponds to the optical thin solution for $\tau = 1$.

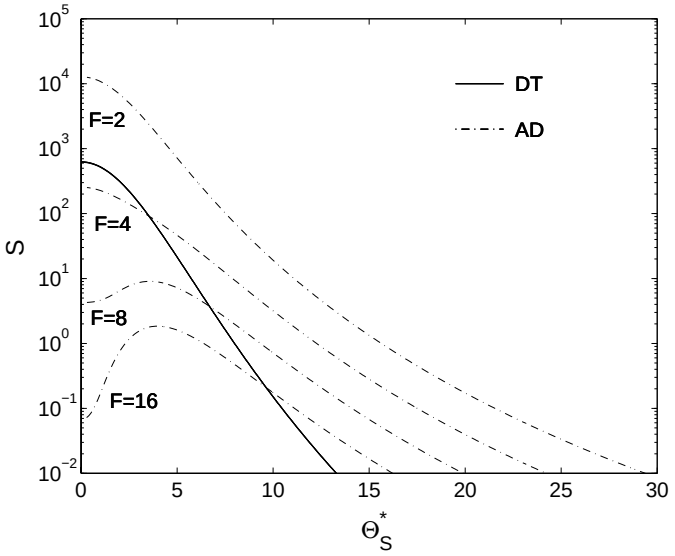

Fig. 4. The beaming pattern, S, for the dust torus (solid line) and the accretion disk (dashed line) as target photon sources in different distances $F = 2, 4, 8$ and 16 (normalised to the accretion disk radius) of the blob from the centre and a bulk Lorentz factor of $\Gamma = 10$; for other parameters, see explanation of Fig. 2: the beaming pattern of the scattered dust torus photons is almost constant whereas the contribution of the accretion disk decreases rapidly with increasing distances F. In the $\Theta_S^* = 0°$ direction the decrease is proportional to F^{-6}. Please note that the beaming pattern shown here is normalised to the luminosity of the actual target photon source, whereas elsewhere in this paper the figures are for a scaling of the target photon luminosities $L_{DT}/L_{AD} = 15$.

The total energy E_{tot} of the electrons in the blob can be obtained from

$$E_{\rm tot} = m_{\rm e}c^2 V_{\rm B} \int_{\gamma_1}^{\gamma_2} {\rm d}\gamma\, \gamma\, n_{\rm e}(\gamma, \Omega_{\rm e}) \quad (42)$$

$$= \frac{m_{\rm e}c^2}{4\pi} V_{\rm B}\, n_{\rm e}^{(0)} \frac{\rho_2}{\rho_1}. \quad (43)$$

We then derive for the beaming pattern in the optically thin case

$$S\Big|_{\rm DT} = \frac{\rho_3}{\rho_2} \frac{E_{\rm tot}}{m_{\rm e}c^2} \frac{\sigma_{\rm T}}{4\tau R_{\rm DT}^2} D^6 \frac{1}{f} \left[\frac{3\mu_{\rm S}^{*2} - 1}{8f^2} {\rm K}_+^{(2)} - 2\frac{\mu_{\rm S}^*}{f} {\rm K}_-^{(1)} + \left(3 - \mu_{\rm S}^{*2} - (1-f^2)\frac{3\mu_{\rm S}^{*2}-1}{2f^2}\right) \ln\left(\frac{o}{u}\right) \right] \quad (44)$$

for the dust torus and

$$S\Big|_{\rm AD} = \frac{\rho_3}{\rho_2} \frac{E_{\rm tot}}{m_{\rm e}c^2} \frac{\sigma_{\rm T}}{R_{\rm AD}^2} D^6 \frac{R_{\rm I}}{R_{\rm AD} - R_{\rm I}} \left[1 - \frac{bR_{\rm S}}{2} \frac{R_{\rm AD} + R_{\rm I}}{R_{\rm AD} R_{\rm I}}\right]^{-1} \times F^{-3} \left[{\rm M}\left(\mu_{\rm S}^*, F\frac{R_{\rm I}}{R_{\rm AD}}\right) - {\rm M}(\mu_{\rm S}^*, F) - \frac{1}{2}\frac{bR_{\rm S}}{R_{\rm AD}F}\left({\rm N}\left(\mu_{\rm S}^*, F\frac{R_{\rm I}}{R_{\rm AD}}\right) - {\rm N}(\mu_{\rm S}^*, F)\right)\right] \quad (45)$$

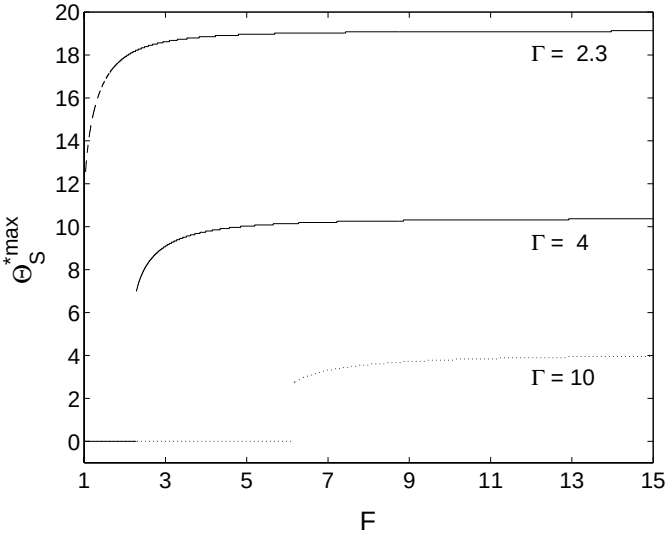

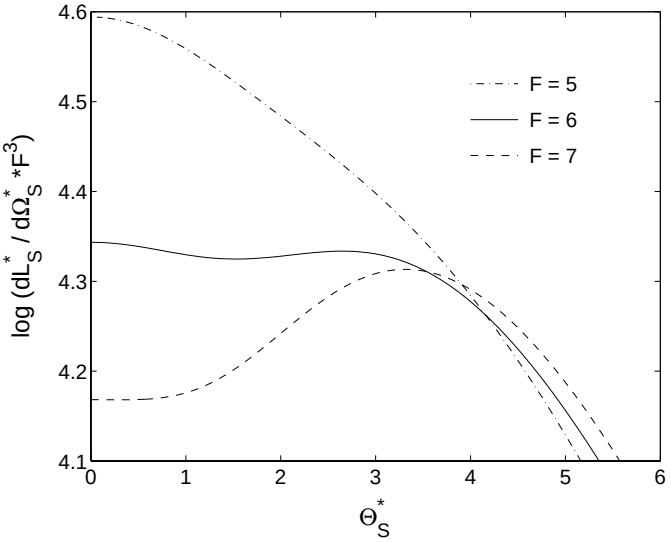

Fig. 5. *Upper panel*: the dependence of the angle of maximum differential luminosity/beaming pattern Θ_S^{*max} on distance F for different blob Lorentz factors Γ. The maximum of the beaming pattern of the scattered accretion disk radiation occurs closer to the jet axis with increasing blob velocities. The minimum in the exact forward direction is established at larger distances with increasing blob velocities. *Lower panel*: the apparent jump of the angle of maximum differential luminosity/beaming pattern in the upper panel occurs because a second maximum establishes with increasing distance. For a Lorentz factor of $\Gamma = 10$ the second maximum becomes the absolut one at a distance of $F \sim 6$. Thus the angle of maximum differential luminosity/beaming pattern Θ_S^{*max} changes at this distance to a value close to 4° as shown in the upper panel.

for the accretion disk. For M and N see (30) and (31), respectively.

Figure 4 shows the beaming pattern for the dust torus (solid line) and the accretion disk (dash-dotted line) as target photon sources in different distances F (normalised to the accretion disk radius) of the blob from the centre in the optically thin case. Here the bulk Lorentz factor is $\Gamma = 10$. The beaming pattern of the scattered dust torus

photons remains almost constant for the considered distances and shows a stronger concentration of the inverse Compton radiation in the forward direction. The contribution of the accretion disk decreases rapidly with increasing distances F and shows a weaker decay with increasing observing angle $\Theta_{\rm S}^*$. The upper panel of Fig. 5 shows the dependence of the angle of maximum differential luminosity/beaming pattern $\Theta_{\rm S}^{*\rm max}$ on distance F for different blob Lorentz factors $\Gamma = 2.3, 4, 10$. The minimum in the forward direction is established at larger distances and the maximum is stronger concentrated towards the jet axis with increasing blob velocities. The lower panel of Fig. 5 illustrates the reason for the apparent jump of the angle of maximum differential luminosity/beaming pattern $\Theta_{\rm S}^{*\rm max}$. With increasing distance an second maximum establishes and in some distance, here $F \sim 6$ for $\Gamma = 10$, becomes the absolute maximum whereas the former one in the forward direction decreases to an absolute minimum.

6. The differential photon number spectrum

Similarly to the calculation of the differential luminosity, the differential photon number spectrum of an extended source can be derived by the integration

$$\dot{N}_{\rm S}^*(\epsilon_{\rm S}^*,\Omega_{\rm S}^*) = D\,V_{\rm B}\int {\rm d}A\;\dot{n}_{\rm S}^* = D\,V_{\rm B}\begin{cases} R_{\rm DT}^2\int\limits_{-\tau}^{\tau}{\rm d}\mu_{\rm T}^*\int\limits_0^{2\pi}{\rm d}\phi_{\rm T}^*\;\dot{n}_{\rm S}^*, & {\rm DT} \\ \int\limits_{R_{\rm I}}^{R_{\rm AD}}{\rm d}R\int\limits_0^{2\pi}{\rm d}\phi_{\rm T}^*\;R\,\dot{n}_{\rm S}^*\;, & {\rm AD.}\end{cases} \tag{46}$$

As seen in the calculation above, the two spectral distributions of the photon source (GB and MC, cf. Eq. (12)) lead to the same differential luminosity. For the monochromatic case an analytic solution for the differential photon number spectrum can be obtained, which we will use henceforth. In the optical thin case, we calculate

$$\dot{N}_{\rm S}^*(\epsilon_{\rm S}^*,\Omega_{\rm S}^*) = \frac{D^2 V_{\rm B}\,\sigma_{\rm T}}{32\,\pi^2}\frac{n_{\rm e}^{(0)}}{\rho_1}\,\epsilon_{\rm S}^{*-\frac{s+1}{2}} \times \begin{cases} \left(\dot{N}_{\rm H}^{(0)}\langle\epsilon^*\rangle^{\frac{s-1}{2}}\right)_{\rm DT} R_{\rm DT}^2\int\limits_{-\tau}^{\tau}{\rm d}\mu_{\rm T}^*\int\limits_0^{2\pi}{\rm d}\phi_{\rm T}^*\;\frac{\eta^{\frac{s+1}{2}}}{x^2}\;, & {\rm DT} \\ \int\limits_{R_{\rm I}}^{R_{\rm AD}}{\rm d}R\int\limits_0^{2\pi}{\rm d}\phi_{\rm T}^*\;R\,\frac{\eta^{\frac{s+1}{2}}}{x^2}\left(\dot{N}_{\rm H}^{(0)}\langle\epsilon^*\rangle^{\frac{s-1}{2}}\right)_{\rm AD}(R), & {\rm AD.}\end{cases} \tag{47}$$

To perform the integrals in (47), we have to take into account that the energy interval of the differential scattering rate $\dot{n}_{\rm S}^*$ in (47) depends on both integration variables (see (15) with (9), (20) and (28)). To perform this we first average η of Eq. (9) over $\phi_{\rm T}^*$

$$\langle\eta\rangle = \frac{1}{2\pi}\int{\rm d}\phi_{\rm T}^*\;\eta(\mu_{\rm H}^*,\phi_{\rm H}^*) = D^2\Big[1-\mu_{\rm S}^*\mu_{\rm H}^*\Big]. \tag{48}$$

Because the system is symmetric to the jet axis this seems to be a good approximation.

The radiation of the counter-jet is highly suppressed because of the angular dependence of the Doppler factor D. For simplicity, we consider aspect angles smaller than $\Theta_{\rm S}^* = 90^\circ$ and distances of the blob smaller than the distance to the torus $f \le 1$.

In the case of the dust torus we obtain for the differential photon number spectrum with the help of Eq. (20) and the substitution $t = \sqrt{1+f^2-2\,f\,\mu_{\rm T}^*}$ the expression

$$\dot{N}_{\rm S}^*\Big|_{\rm DT} = \frac{V_{\rm B}\,\sigma_{\rm T}\,\dot{N}_{\rm H}^{(0)}\big|_{\rm DT}}{32\,\pi^2}\,\frac{n_{\rm e}^{(0)}}{\rho_1}\,\langle\epsilon^*\rangle_{\rm DT}^{\frac{s-1}{2}}\,D^{s+3}\,\epsilon_{\rm S}^{*-\frac{s+1}{2}} \times\frac{1}{f}\int{\rm d}t\;\frac{\left[\mu_{\rm S}^*\,(1-f^2)+2\,f\,t-\mu_{\rm S}^*\,t^2\right]^{\frac{s+1}{2}}}{(2\,f)^{\frac{s+1}{2}}\,t^{\frac{s+3}{2}}}. \tag{49}$$

The lower limit for $\epsilon_{\rm S}^*$ in (15) lead with (20) to the restrictions for the new integration variable t

$$(t-t_{\gamma_1}^+)\,(t-t_{\gamma_1}^-) \ge 0 \tag{50}$$

with

$$t_{\gamma_1}^{\pm} = \frac{f}{\mu_{\rm S}^*}\left(1-\frac{\epsilon_{\rm S}^*}{D^2\,\langle\epsilon^*\rangle_{\rm DT}\,{\gamma_1}^2}\right) \pm\sqrt{\frac{f^2}{{\mu_{\rm S}^*}^2}\left(1-\frac{\epsilon_{\rm S}^*}{D^2\,\langle\epsilon^*\rangle_{\rm DT}\,{\gamma_1}^2}\right)^2+1-f^2} \tag{51}$$

and the upper limit for $\epsilon_{\rm S}^*$ leads to

$$(t-t_{\gamma_2}^+)\,(t-t_{\gamma_2}^-) \le 0 \tag{52}$$

with

$$t_{\gamma_2}^{\pm} = \frac{f}{\mu_{\rm S}^*}\left(1-\frac{\epsilon_{\rm S}^*}{D^2\,\langle\epsilon^*\rangle_{\rm DT}\,{\gamma_2}^2}\right) \pm\sqrt{\frac{f^2}{{\mu_{\rm S}^*}^2}\left(1-\frac{\epsilon_{\rm S}^*}{D^2\,\langle\epsilon^*\rangle_{\rm DT}\,{\gamma_2}^2}\right)^2+1-f^2}. \tag{53}$$

For $f < 1$ the "–"-solution becomes negative and can excluded because by definition t represents a distance. Taking this together we get

$$t_{\gamma_1}^+ \;\le\; t \;\le\; t_{\gamma_2}^+\,. \tag{54}$$

Outside of this interval the integrand becomes zero. For the indefinite integral in (49) no general solution can be found. To get a first result, we assume that the spectral index of the electron distribution is $s = 3$.

The two limits in (54) can be inside or outside the integration interval

$$[\sqrt{1+f^2-2\,f\,\tau},\sqrt{1+f^2+2\,f\,\tau}] \;\equiv\; [T_-,T_+], \tag{55}$$

respectively. If they are inside we had to change the integration limits. So after integration the solution for the differential photon number spectrum is split into three parts.

$$\dot{N}_{\rm S}^*\Big|_{\rm DT} = \frac{V_{\rm B}\,\sigma_{\rm T}\left(\dot{N}_{\rm H}^{(0)}\langle\epsilon^*\rangle\right)_{\rm DT}}{32\,\pi^2}\,\frac{n_{\rm e}^{(0)}}{\rho_1}\,D^6\,{\epsilon_{\rm S}^*}^{-2}\,\frac{1}{f}$$
$$\times\left[\frac{{\mu_{\rm S}^*}^2}{8\,f^2}\,{\rm K}_+^{(2)} - \frac{\mu_{\rm S}^*}{2f}{\rm K}_-^{(1)} + \left(1-\frac{{\mu_{\rm S}^*}^2}{2\,f^2}(1-f^2)\right)\ln\left(\frac{o}{u}\right)\right]$$
$$\text{with}\quad \left\{\begin{array}{ll} o=T_+ \\ u=t_{\gamma_1}^+ \end{array}\right\}\ \text{for}\quad {\gamma_1}^2\,A_+ \le \epsilon_{\rm S}^* \le {\gamma_1}^2\,A_- \qquad (56)$$
$$\left\{\begin{array}{ll} o=T_+ \\ u=T_- \end{array}\right\}\ \text{for}\quad {\gamma_1}^2\,A_- \le \epsilon_{\rm S}^* \le {\gamma_2}^2\,A_+$$
$$\left\{\begin{array}{ll} o=t_{\gamma_2}^+ \\ u=T_- \end{array}\right\}\ \text{for}\quad {\gamma_2}^2\,A_+ \le \epsilon_{\rm S}^* \le {\gamma_2}^2\,A_-.$$

For clarity we defined the functions $A_\pm = A_\pm(f,\mu_{\rm S}^*)$,

$$A_\pm \equiv D^2\,\langle\epsilon^*\rangle_{\rm DT}\left(1-\mu_{\rm S}^*\,\frac{f\pm\tau}{\sqrt{1+f^2\pm 2\,f\,\tau}}\right), \qquad (57)$$

which carry the information about the position of the blob and the aspect angle. For the definition of $t_{\gamma_{1|2}}^+$, $T_\pm$ and ${\rm K}_\pm^{(n)}$ see (51), (53), (55) and (22).

Again, in the optically thick case the cosine $\mu_{\rm K}^*$, defined in (33), has to be added to the integrand in (46). Note that the limits in (56) are not affected. In comparison to the optically thin solution in the second line in (56) changes to

$$\frac{1}{2}\left[\frac{{\mu_{\rm S}^*}^2}{12f^2}\,{\rm K}_+^{(3)} - \frac{\mu_{\rm S}^*}{2f}\,{\rm K}_-^{(2)} + \left(1-\frac{{\mu_{\rm S}^*}^2}{4f^2}(1-f^2)\right){\rm K}_+^{(1)}\right]. \qquad (58)$$

For the accretion disk we get for $s=3$ and optically thin emission with the help of (20), (28), (48) and the substitution $y=z/R$

$$\dot{N}_{\rm S}^*\Big|_{\rm AD} = \frac{3qV_{\rm B}\,\sigma_{\rm T}}{256\,\pi^3 R_{\rm AD}^3}\,\frac{n_{\rm e}^{(0)}}{\rho_1}\,D^6\,{\epsilon_{\rm S}^*}^{-2}\,\frac{GM_\odot^2}{m_{\rm e}c^2 a}\left(\frac{M}{M_\odot}\right)\left(\frac{\dot{M}}{M_\odot/a}\right)$$
$$\times\ F^{-3}\int_F^{F\frac{R_{\rm AD}}{R_{\rm I}}}{\rm d}y\ y^2\,\frac{(\sqrt{1+y^2}-\mu_{\rm S}^* y)^2}{(1+y^2)^2}\left(1-\frac{bR_{\rm S}}{FR_{\rm AD}}\,y\right) \qquad (59)$$

with the additional restriction in energy

$$\epsilon_{\gamma_1}^* \le \epsilon_{\rm S}^* \le \epsilon_{\gamma_2}^*,$$
$$\epsilon_{\gamma_{1|2}}^* \equiv \left(1-\mu_{\rm S}^*\frac{y}{\sqrt{1+y^2}}\right)\langle\epsilon^*\rangle_{\rm AD}(y)D^2\,\gamma_{1|2}^2, \qquad (60)$$

where $\langle\epsilon^*\rangle_{\rm AD}(y)$ is derived with (13) and the Stefan-Boltzmann law

$$\langle\epsilon^*\rangle_{\rm AD}(y) = 3\frac{\zeta(4)}{\zeta(3)}\frac{k_{\rm B}}{m_{\rm e}c^2}\left(\frac{B(y)}{\sigma_{\rm SB}}\right)^{\frac{1}{4}}. \qquad (61)$$

For $B(y)$ see (25) with $R=z/y$. The energy restriction in (60) leads to energy dependent arguments which can be specified numerically. To get an analytical expression for the energy dependent integration limits, we set $\varphi\equiv 1$ and consider distances $F>1$. For the two important cases $\mu_{\rm S}^*=1$ and $F\gg 1$ the energy restriction can be approximated accurately. We expand

$$\mu_{\rm H}^* = \frac{y}{\sqrt{1+y^2}} = 1-\frac{1}{2y^2}+\mathcal{O}\left(\frac{1}{y^4}\right) \qquad (62)$$

and derive the explicit restrictions for y.

Case Ⓐ: $\mu_{\rm S}^*=1$.

In the case $\mu_{\rm S}^*=1$ the first order expansion of $\mu_{\rm H}^*$ is an accurate approximation for all values of F slightly larger than 1. With

$$C\equiv 3\frac{\zeta(4)}{\zeta(3}\frac{k_{\rm B}}{m_{\rm e}c^2}\left(\frac{3}{8\pi}\frac{GM_\odot^2}{\sigma_{\rm SB}a}\right)^{\frac{1}{4}}\left(\frac{M}{M_\odot}\right)^{\frac{1}{4}}\left(\frac{\dot{M}}{M_\odot/a}\right)^{\frac{1}{4}}R_{\rm AD}^{-\frac{1}{2}} \qquad (63)$$

we get for the integration variable y

$$y_1^{(A)} \le y \le y_2^{(A)},\quad y_{1|2}^{(A)} \equiv \left(\frac{D^2C\gamma_{1|2}^2}{2\,\epsilon_{\rm S}^*}\right)^{\frac{4}{5}}F^{-\frac{3}{5}}. \qquad (64)$$

In comparison to the numerically achieved value, the lower cut-off takes place at higher energies (cf. Fig. 6).

Case Ⓑ: $F\gg 1$.

In a distance $F>10$ most of the target photons penetrate the blob from behind. At high energies the approximation $\mu_{\rm H}^* = y/\sqrt{1+y^2}\equiv 1$ shifts the cut-off to slightly higher energies (cf. Fig. 7). Considering aspect angles $\Theta_{\rm S}^*>20^\circ$ the approximation also holds for $F<10$. We obtain

$$y_2^{(B)} \le y \le y_1^{(B)},\ y_{1|2}^{(B)} \equiv \left(\frac{\epsilon_{\rm S}^*}{D^2C\gamma_{1|2}^2}\frac{1}{1-\mu_{\rm S}^*}\right)^{\frac{4}{3}}F. \qquad (65)$$

We define the new functions

$$\tilde{\rm M}(\mu_{\rm S}^*,y) \equiv (1+{\mu_{\rm S}^*}^2)\,y - 2\mu_{\rm S}^*\frac{y^2+2}{\sqrt{1+y^2}}$$
$$-\ \frac{1}{2}(3{\mu_{\rm S}^*}^2+2)\arctan(y) + \frac{1}{2}\,{\mu_{\rm S}^*}^2\frac{x}{1+y^2}, \qquad (66)$$

$$\tilde{\rm N}(\mu_{\rm S}^*,y) \equiv (1+{\mu_{\rm S}^*}^2)\,y^2 - 2\mu_{\rm S}^*\left[\frac{y(y^2+3)}{\sqrt{1+y^2}} - 3\,{\rm arcsinh}(y)\right]$$
$$-\ (2{\mu_{\rm S}^*}^2+1)\ln(1+y^2) - {\mu_{\rm S}^*}^2\frac{1}{1+y^2}. \qquad (67)$$

which are slightly different to M and N in (30) and (31), respectively, and we get for the differential photon number spectrum $\dot{N}_{\rm S}^*$

$$\dot{N}_{\rm S}^*\Big|_{\rm AD} = \frac{3q}{296\,\pi^3}V_{\rm B}\,\sigma_{\rm T}\,\frac{n_{\rm e}^{(0)}}{\rho_1}\,D^6\,{\epsilon_{\rm S}^*}^{-2}\left(\frac{GM_\odot^2}{m_{\rm e}c^2a}\right)R_{\rm AD}^{-3}\,F^{-3}$$
$$\times\ \left(\frac{M}{M_\odot}\right)\left(\frac{\dot{M}}{M_\odot/a}\right)\Big[\tilde{\rm M}(\mu_{\rm S}^*,o)-\tilde{\rm M}(\mu_{\rm S}^*,u)$$
$$-\ \frac{1}{2}\,\frac{bR_{\rm S}}{R_{\rm AD}\,F}\left(\tilde{\rm N}(\mu_{\rm S}^*,o)-\tilde{\rm N}(\mu_{\rm S}^*,u)\right)\Big]$$

with

$$\text{Ⓐ} \quad \begin{cases} o = F/q \\ u = x_1^{(A)} \end{cases} \Big\} \text{ for } U_{\gamma_1} q^{\frac{5}{4}} \leq \epsilon_{\rm S}^* \leq U_{\gamma_1}$$
$$\begin{cases} o = F/q \\ u = F \end{cases} \Big\} \text{ for } U_{\gamma_1} \leq \epsilon_{\rm S}^* \leq U_{\gamma_2} q^{\frac{5}{4}} \quad (68)$$
$$\begin{cases} o = x_2^{(A)} \\ u = F \end{cases} \Big\} \text{ for } U_{\gamma_2} q^{\frac{5}{4}} \leq \epsilon_{\rm S}^* \leq U_{\gamma_2}$$

$$\text{Ⓑ} \quad \begin{cases} o = x_1^{(B)} \\ u = F \end{cases} \Big\} \text{ for } V_{\gamma_1} \leq \epsilon_{\rm S}^* \leq V_{\gamma_1}/q^{\frac{3}{4}}$$
$$\begin{cases} o = F/q \\ u = F \end{cases} \Big\} \text{ for } V_{\gamma_1}/q^{\frac{3}{4}} \leq \epsilon_{\rm S}^* \leq V_{\gamma_2} \quad (69)$$
$$\begin{cases} o = F/q \\ u = x_2^{(B)} \end{cases} \Big\} \text{ for } V_{\gamma_2} \leq \epsilon_{\rm S}^* \leq V_{\gamma_2}/q^{\frac{3}{4}},$$

where $q = R_{\rm I}/R_{\rm AD}$ is the quotient of the inner and the outer accretion disk radius and $U_{\gamma_{1|2}} = U_{\gamma_{1|2}}(F)$ and $V_{\gamma_{1|2}} = V_{\gamma_{1|2}}(F, \mu_{\rm S}^*)$ are defined as

$$U_{\gamma_{1|2}} \equiv \frac{D^2(\mu_{\rm S}^* = 1) C \gamma_{1|2}^2}{2F^2}, \quad (70)$$

$$V_{\gamma_{1|2}} \equiv D^2 C \gamma_{1|2}^2 (1 - \mu_{\rm S}^*). \quad (71)$$

For the definition of $y_{\gamma_{1|2}}^{(A|B)}$ see (64) and (65).

We supplement $\mu_{\rm K}^*$ in (59) to get the solution for optically thick accretion disk emission. The solution corresponds to the optically thin solution when $\tilde{\rm M}$ is replaced by $\tilde{\rm P}$ and $\tilde{\rm N}$ by $\tilde{\rm Q}$, respectively, with

$$\tilde{\rm P}(\mu_{\rm S}^*, y) \equiv (1 + {\mu_{\rm S}^*}^2) \frac{y^2 + 2}{\sqrt{1 + y^2}} - \frac{1}{3} {\mu_{\rm S}^*}^2 \frac{3y^2 + 2}{(1 + y^2)^{\frac{3}{2}}} - 2\mu_{\rm S}^* \left[y + \frac{1}{2} \frac{y}{1 + y^2} - \frac{3}{2} \arctan(y) \right], \quad (72)$$

$$\tilde{\rm Q}(\mu_{\rm S}^*, y) \equiv (1 + {\mu_{\rm S}^*}^2) \frac{y(y^2 + 3)}{\sqrt{1 + y^2}} - (4{\mu_{\rm S}^*}^2 + 3) \operatorname{arcsinh}(y) - 2\mu_{\rm S}^* \left[y^2 + \frac{1}{1 + y^2} - 2\ln(1 + y^2) \right] + \frac{1}{2}(3{\mu_{\rm S}^*}^2 - 1) \left[\frac{1}{3} \frac{y^3}{(1 + y^2)^{\frac{3}{2}}} + \frac{y}{\sqrt{1 + y^2}} \right]. \quad (73)$$

The different dependences on the distance of the blob F and the angle $\Theta_{\rm S}^*$ between the jet axis and the observer for the two considered target photon sources in the case of optically thin emission are illustrated by Figs. 6 and 7. We use $\gamma_1 = 100$ and $\gamma_2 = 10^5$ for the lower and the upper limit of the electron spectrum, respectively. The blob Lorentz factor is $\Gamma = 10$; for other parameters, see explanation to Fig. 2.

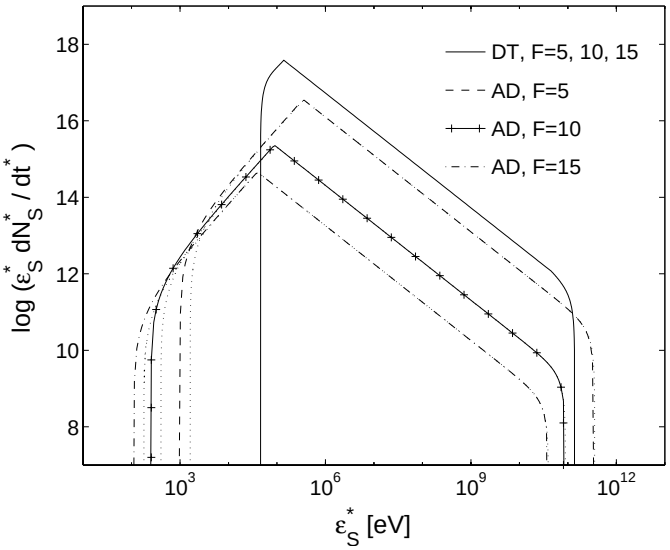

Fig. 6. The differential intensity spectrum of the inverse-Compton scattered photons for the dust torus and the accretion disk as target-photon sources in arbitrary units derived by numerically quantified integration limits. The dotted lines associated to the different spectra present the approximated analytical solutions. The aspect angle is 0°, the lower and the upper limit of the electron spectrum $\gamma_1 = 100$ and $\gamma_2 = 10^5$, respectively. The blob Lorentz factor is $\Gamma = 10$. The dotted lines associated to the different spectra present the approximated analytical solution For other parameters, see explanation of Fig. 2. When comparing to Fig. 4 please note that this figure is derived for a scaling $L_{\rm DT}/L_{\rm AD} = 15$. Varying the distance of the blob of relativistic electrons from the central black hole, F, measured in units of the accretion disk radius, we see that the intensity of scattered radiation disk emission falls of strongly whereas that of the scattered dust radiation remains constant.

Figure 6 shows the results for the differential intensity spectrum for the dust torus and the accretion disk as target-photon sources in the distances of 5, 10 and 15 accretion disk radii, respectively. The dotted lines associated to the different spectra represent the approximated analytical "accretion disk"-solutions. The aspect angle is 0°. The spectrum of scattered dust emission is nearly constant (up to $F \sim 100$) whereas the scattered accretion disk emission decreases by two orders of magnitude.

The sharp peak and the inversion of the spectrum at small energies results at least partly from the head-on approximation for the inverse Compton cross Sect. (2). Because of the low energy cut-off in the electron spectrum, γ_1, the energy condition, represented by the delta functional in (2), can not be satisfied for all relevant scattering angles. This means that only some part of the target photon distribution, actually those penetrating the blob from favourable directions, can be scattered to become γ-rays of very low energies. The geometrical restrictions still being present, the use of the full scattering cross section would result in a smooth turn-over of the intensity spectrum at low γ-ray energies.

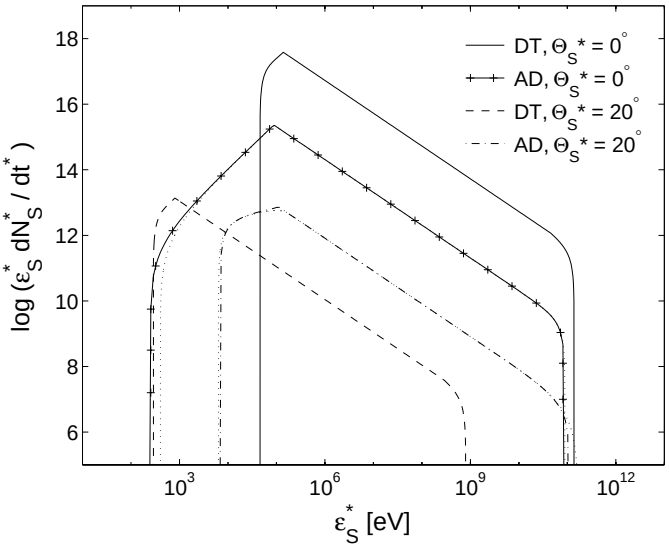

Fig. 7. The differential intensity spectrum of the inverse-Compton scattered photons in arbitrary units for a blob distance $F = 10$, an aspect angle of 0° (solid and solid & crosses line) and 20° (dashed and the dash-dotted line) for the dust torus (DT) and the accretion disk (AD), respectively. The dotted lines associated to the different spectra of comptonised accretion disk emission present the approximated analytical solutions. The accretion disk contribution shows a weaker dependence on the observing angle $\Theta_{\rm S}^*$: at intermediate aspect angles the scattered accretion disk emission can dominate the spectrum, though close to the jet axis the scattered dust emission is nearly two orders of magnitude stronger than the scattered accretion disk radiation. Note again that in this figure we have assumed $L_{\rm DT}/L_{\rm AD} = 15$.

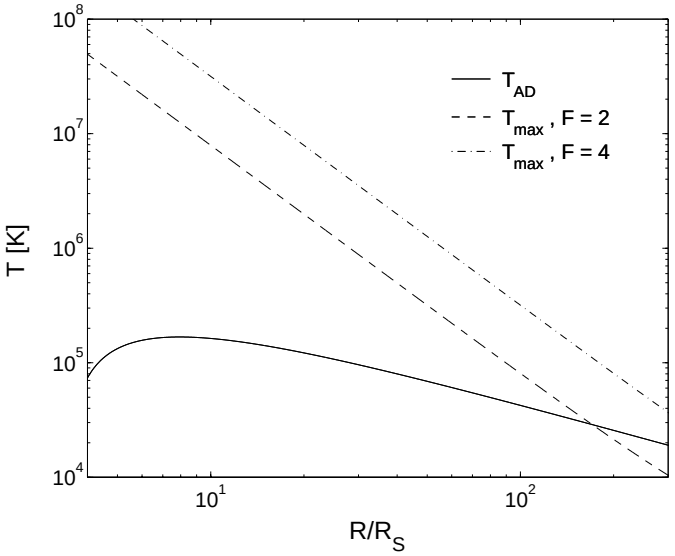

Fig. 8. Radial temperature distribution of the accretion disk (solid line) for a black hole of $M = 10^8 M_\odot$ and upper limits for $F = 2$ (dashed line) and $F = 4$ (dash-dotted line) for the validity of the Thomson limit.

The angular dependences of the differential intensity spectrum are displayed in Fig. 7: for a distance of $F = 10$ the dashed and the dash-dotted line show the differential intensity spectrum for an aspect angle of 20°, the solid and the solid&crosses line for an aspect angle of 0° for the dust torus (DT) and the accretion disk (AD), respectively. The dotted lines associated to the different spectra of comptonised accretion disk photons represent the approximated analytical solutions. Again, the superposition of relativistic motion and geometrical properties leads to a different angular dependence in the two considered cases of target photon sources.

7. The Thomson limit

We use the differential cross section $\mathrm{d}^2\sigma/(\mathrm{d}\epsilon_{\rm S}\mathrm{d}\Omega_{\rm S})$ in the Thomson limit $\epsilon' \leq 1$. Applied to the monochromatic approximation, the energy restriction transformed into the galactic rest frame leads to

$$\langle\epsilon^*\rangle \leq \left[\gamma\Gamma(1-\beta\psi)(1-B_\Gamma\mu_{\rm H}^*)\right]^{-1}. \quad (74)$$

This limitation is most severe for head-on collisions, i.e. $\psi = -1$. Moreover setting $B_\Gamma = \beta = 1$ we get

$$\langle\epsilon^*\rangle \leq \left[2\gamma\Gamma(1-\mu_{\rm H}^*)\right]^{-1}. \quad (75)$$

For the different target photon sources we deal with, the lowest energies are required for the largest values of $\Theta_{\rm H}^*$, i.e. for photons emitted at the upper edge of the dust distribution, $\mu_{\rm H}^* = -\tau$, and the outer rim of the accretion disk, $\mu_{\rm H}^* = 1/\sqrt{1+F^{-2}}$, respectively. If we allow for a closed dust sphere, $\tau = 1$, we get as Thomson limit for the target photon energy and the corresponding temperature $T_{\rm DT} = m_{\rm e}c^2/k_{\rm B}\cdot\zeta(3)/(3\zeta(4))\cdot\langle\epsilon^*\rangle_{\rm DT}$

$$\langle\epsilon^*\rangle_{\rm DT} \leq 2.5\times10^{-7}, \quad T_{\rm DT} \leq 550\ \mathrm{K} \quad (76)$$

with $\gamma \equiv \gamma_2 = 10^5$ and $\Gamma = 10$. Thus the Thomson limit is applicable for dust emission below 550 K.

We consider distances of the blob larger than one accretion disk radius, $F > 1$, and presented results for $F \geq 5$. In Fig. 8 we compare the radial temperature distribution of the accretion disk (solid line) for a black hole of $M = 10^8 M_\odot$ with the values allowed by the Thomson limit. For a distance of $F = 2$ (dashed line) the Thomson limit is violated for $R > 100\ R_{\rm S}$ whereas for distances of $F \geq 4$ (dash-dotted line) the use of the Thomson limit is always justified. Note that the distance $F = z/R_{\rm AD}$ scales with the accretion disk radius. Thus if we consider more extended accretion disks with $R_{\rm AD} > 300\ R_{\rm S}$ the applicability for $F \geq 4$ is still granted. The temperature distribution, represented in dependence of the normalised Radius $R/R_{\rm S}$ scales with $(M/M_\odot)^{-1/2}$ (cf. Eq. (25)). Therefore the use of the Thomson limit for $M/M_\odot < 10^8$ is still valid for $F \gg 1$.

8. Summary and discussion

In this paper we have calculated comptonisation γ-ray spectra of AGNi for arbitrary observing angles. We present analytical solutions for the bolometric luminosity, the beaming pattern and the photon number spectrum

produced by inverse-Compton scattering for an arbitrarily placed point source of target photons as well as for the accretion disk and a dust torus as the target photon source for optically thick and thin emission. Our study does not rely on a specific model for the injection or acceleration of relativistic electrons in the jets of AGN. Therefore our results can also be used to determine EIC spectra in blast wave models for AGN and GRB (e.g. Pohl & Schlickeiser 2000).

In agreement with previous studies, our results show that the highest differential luminosity and photon energy is emitted along the jet axis and for small distances to the accretion disk. Moreover, we point out that the scattered dust emission is concentrated on small aspect angles, whereas the scattered accretion disk photons show a broader distribution in aspect angle. For small aspect angles the relative relevance of the dust torus and the accretion disk depends sensitively on the distance of the blob from the accretion disk. Thus for small angles to the jet axis and distances of more than a few accretion disk radii the dust surrounding the AGNi is more important as target photon source for the inverse-Compton scattering.

The presented model for comptonisation of external photon fields does in principle also apply for the broad line region (BLR) as target photon source. It can be treated either as a homogeneous sphere with a photon emission rate determined by the total luminosity of the BLR, analogously to the approach for the dust torus, or as discrete point sources (clouds), thus as a summation of point source solutions also presented in this paper. However, the comptonisation of the BLR photons does not always happen in the Thomson regime, therefore our analytical approach is not always applicable for all γ-ray energies. Numerical solutions of the comptonisation of BLR photons using the full Bethe-Heitler cross section have been presented by Böttcher & Bloom (2000). The relative influence of the dust emission in comparison to the emission of the BLR depends sensitively on the strength of the energy density of the photon fields and the proportions of the emitters. For distances $z \gg R_{\rm BLR}$ the photon field of the BLR decays with the distance squared, thus we expect the dust to be the dominant target photon source at least in this regime.

Though our results are not directly comparable with the time-averaged spectra presented by Błażejowski et al. (2000) for a specific line-of-sight to the observer ($\theta_{\rm obs} = 1/\Gamma$) our results confirm the relative importance of the dust on the inverse Compton radiation at least for AGN known as strong infra-red sources. The weak dependence of the comptonised dust emission for distances less than $F \sim 100$ for $\tau = 0.5$ and even further for a more closed dust configuration seems to justify the assumption of a constant energy density $u_{\rm IR}$ used by Błażejowski et al. in the range $z \ll R_{\rm DT}\tau$.

A strong external photon field is likely to be found in FSRQ/OVV, in contrast to the case of BL Lacs. It may be concluded that the FSRQ/OVV observed with EGRET, i.e. the brightest ones, are those seen nearly head-on, in which case we probably observe comptonised dust emission. The FSRQ/OVV seen at an intermediate angle $\Theta^* \approx 10^\circ$ would show a significant level of scattered accretion disk emission. The latter objects are less intense, meaning they would be less likely identified as point sources, but would contribute to the extragalactic γ-ray background (Sreekumar et al. 1998).

Acknowledgements. We gratefully acknowledge financial support by the Bundesministerium für Bildung und Forschung through DESY, grant Verbundforschung 05AG9PCA.

References

Bednarek, W., & Kirk, J. G. 1995, A&A, 294, 366
Begelman, M. C., Blandford, R. D., & Rees, M. J. 1984, Rev. Mod. Phys., 56, 255
Böttcher, M., & Bloom, S. D. 2000, A&A, 119, 469
Błażejowski, M., Sikora, M., Moderski, R., & Madejski, G. M. 2000, ApJ, 545, 107
Catanese, M., Akerlof, C. W., Badran, H. M., et al. 1998, ApJ, 501, 616
Cohen, M. H., Linfield, R. P., Moffet, A. T., et al. 1977, Nature, 268, 405C
Coppi, P. S., & Aharonian, F. A. 1999, ApJ, 521, L33
Dermer, C. D., Schlickeiser, R., & Mastichiadis, A. 1992, A&A, 256, L27
Dermer, C. D., & Schlickeiser, R. 1993, ApJ, 416, 458
Ghisellini, G., Celotti, A., Fossati, G., et al. 1998, MNRAS, 301, 451
Gómez, J. L., Marscher, A. P., Alberdi, A., et al. 1998, ApJ, 499, 221
Gradshteyn, I. S., & Ryzhik, I. M. 1965, Table of integrals, series and products, fourth edition (New York – London: Academic Press)
Hagedorn, R. 1973, Relativistic Kinematics, third printing (Massachusetts: W. A. Benjamin, Inc.)
Haas, M., Chini, R., Meisenheimer, K., et al. 1998, ApJ, 503, L109
Haas, M., Müller, S. A. H., Chini, R., et al. 2000, A&A, 354, 453
Krennrich, F., Akerlof, C. W., Buckley, J. H., et al. 1997, ApJ, 481, 758
Maraschi, L., Ghisellini, G., & Celotti, A. 1992, ApJ, 397, L5
Mastichiadis, A., & Kirk, J. G. 1997, A&A, 320, 19
Mukherjee, R., Bertsch, D. L., Bloom, S. D., et al. 1997, ApJ, 490, 116
Pohl, M., & Schlickeiser, R. 2000, A&A, 354, 395
Protheroe, R. J., & Biermann, P. L. 1997, APh, 6, 293
Punch, M., Akerlof, C. W., Cawley, M. F., et al. 1992, Nature, 358, 477
Quinn, J., Akerlof, C. W., Biller, S., et al. 1996, ApJ, 456, L83
Reynolds, G. B. 1982, ApJ, 256, 38
Rybicki, G. B., & Lightman, A. P. 1979, Radiative Processes in Astrophysics (New York: John Wiley & Sons)
Schmidt, M. 1963, Nature, 197, 1040
Shakura, N. I., & Sunyaev, R. A. 1973, A&A, 24, 337
Sikora, M., Begelman, M. C., & Rees, M. J. 1994, ApJ, 421, 153
Sreekumar, P., Bertsch, D. L., Dingus, B. L., et al. 1998, ApJ, 494, 523
Urry, C. M., & Padovani, P. 1995, PASP, 107, 803
von Montigny, C., Bertsch, D. L., Chiang, J., et al. 1995, ApJ, 440, 525